


Ferroelectric domain wall clusters in perfectly screened barium titanate type systemsChris Halcrow^{*} and Egor Babaev*Department of Physics, KTH-Royal Institute of Technology, SE-10691, Stockholm, Sweden* (Received 15 June 2023; revised 14 September 2023; accepted 9 October 2023; published 2 November 2023)

We study ferroelectric domain walls in barium titanate-type systems with perfect electric screening. We search for structurally nontrivial so-called non-Ising domain walls, where the polarization is nontrivial for all components. Our approach enables us to find solutions for domain walls in any orientation, and the existence and energy of these walls depend on their particular orientation. We find that, across all phases of the material, there are orientations where the non-Ising walls have lower energy than Ising walls. The most interesting property of these domain walls is their nonmonotonic interaction forces, allowing them to form stable domain-wall clusters rather than following standard behavior where domain walls annihilate or repel each other. We find the required external electric field to create the non-Ising configurations. Besides theoretical interest, this unconventional property of domain walls makes them a good candidate for memory applications.

DOI: [10.1103/PhysRevB.108.174101](https://doi.org/10.1103/PhysRevB.108.174101)**I. INTRODUCTION**

Domain walls (DWs) are ubiquitous in ferroelectric materials. In an Ising wall, the most common type, the electric polarization has a single component, proportional to the boundary polarization. It was once thought that all DWs in barium titanate were Ising, but more recent theory has predicted the existence of exotic walls in different phases of the material. Often, the polarization vector rotates orthogonal to or along with the domain walls, making them analogous to Bloch and Néel walls in magnetic systems. There are high-energy Bloch walls in the tetragonal phase [1] and low-energy non-Ising walls in the rhombohedral phase [2], novel “non-Ising” DWs have been theoretically predicted [3,4], and reported experimentally [5,6]. Complicated structures such as achiral [7] and bichiral [8] walls have also been predicted; the second due to flexoelectric coupling. The energy of all walls mentioned here depends on their orientation, showing the importance of geometric considerations.

The diversity, robustness, mobility, and sharpness of their domain walls make ferroelectrics candidates for promising new technological applications. One significant application is in memory, where the presence or absence of the DW can represent the binary state. The creation and nondestructive readability of DW states has been demonstrated in various systems [9–12]. Hence ferroelectrics represent not only an academically interesting platform to search for new kinds of topological defects, but also have great potential for new

applications. However, DW-racetrack memory has a major drawback compared to other technologies: pairs of domain walls are generically unstable to annihilation. Usually, it is assumed that the DWs are pinned to a defect or kept apart to avoid this instability.

In this paper, we report the existence of stable wall-wall pairs and clusters in our model of “perfectly-screened” barium-titanate-type systems. For brevity, we refer to our model below barium titanate. The screening assumption means that we ignore electrostatic effects. One can model the electrostatics by following Ishibashi and Salje [13], or by considering depolarization fields [7], but we ignore it so that we can consider walls in arbitrary orientations. The clusters studied here are localized on domain walls. Hence in a three-dimensional material, they are localized on two-dimensional planes.

In soliton language, the clusters are constructed from soliton-antisoliton pairs. Stable configurations of this type with net zero topological charge are incredibly rare in condensed matter. Some examples are skyrmionium and skyrme bags, made from a placing skyrmions inside an antiskyrmion, which have been predicted and observed in magnetic systems [14–18] and stable vortex-antivortex excitations which have been generated numerically in a spin imbalanced superfluid [19] and noncentrosymmetric superconductors [20,21]. Some higher-dimension dimensional solitons can be interpreted as composite lower-dimensional soliton-antisolitons, such as skyrmions in the form of co-centric domain and anti-domain-wall rings decorated by vortices in certain superconductors [22]. In that example the decoration of domain walls by vortices enforces the stability. We are not aware of a condensed matter example of systems allowing energetically stable domain-antidomain-wall structures. In ferroelectrics there are examples of stable wall-wall pairs in periodic systems [2,23,24], but these boundary conditions stabilize pairs which repel each other. Ours attract at long range and are thus true local minima. The stability of the domain wall clusters

*chalcrow@kth.se

that we find crucially relies on the wall's non-Ising character and the geometry of the system.

To study these configurations, we first generalize the Ginzburg-Landau-Devonshire formalism of Ref. [25] to consider walls with arbitrary orientations. We demonstrate that there are wall orientations which support non-Ising DWs in every phase. We also demonstrate how the stable configurations can be created using an external electric field. During our analysis, we adapt several tools from soliton theory to the field of ferroelectrics. These include arrested Newton flow, the string method and a small-fluctuation gradient flow. We aim to explain these methods in a clear and general manner, so that they can be readily applied to problems in higher dimensions.

II. THEORETICAL FRAMEWORK

The Ginzburg-Landau-Devonshire model of ferroelectrics features the polarization vector $\mathbf{P} = (P_1, P_2, P_3)$ and the symmetric 3×3 strain tensor u_{ij} as order parameters. Throughout derivatives are denoted by $\frac{\partial}{\partial x_a} = \partial_a$ and we sum over repeated indices. We study a free energy which is compatible with the symmetries of the underlying crystal. In our case, the goal is to minimize the free energy given by

$$F = \frac{1}{2} G_{abcd}^o \partial_a P_b \partial_c P_d + V^o(P) + \frac{1}{2} C_{abcd}^o u_{ab} u_{cd} - q_{abcd}^o u_{ab} P_c P_d$$

$$V^o = A_{ab}^o P_a P_b + A_{abcd}^o P_a P_b P_c P_d + A_{abcdef}^o P_a P_b P_c P_d P_e P_f$$

subject to the elastic compatibility condition

$$\mathcal{D}u = \epsilon_{acd} \epsilon_{bef} \partial_c \partial_e u_{df} = 0. \quad (1)$$

We use the superscript ‘‘o’’ to mean ‘‘original coordinates.’’

We will sometimes use Voigt notation for the strain tensor. Here, we reshape the symmetric matrix u into a 6-vector

$$(\epsilon_1, \epsilon_2, \epsilon_3, \epsilon_4, \epsilon_5, \epsilon_6) = (u_{11}, u_{22}, u_{33}, 2u_{23}, 2u_{13}, 2u_{12}). \quad (2)$$

Latin and Greek letters are used when summing over the old and new subscripts, so that $a = 1, 2, 3$ but $\alpha = 1, \dots, 6$. Provided the tensors are symmetrized, the Voigt coefficients are uniquely defined by

$$C_{\alpha\beta}^o \epsilon_\alpha \epsilon_\beta = C_{abcd}^o u_{ab} u_{cd}, \quad (3)$$

$$q_{\alpha cd}^o \epsilon_\alpha = q_{abcd}^o u_{ab}. \quad (4)$$

Using this notation, we can immediately complete the square on the part of F that depends on strain, which becomes

$$\frac{1}{2} C_{\alpha\beta}^o (\epsilon_\alpha - Q_{\alpha ef}^o P_e P_f) (\epsilon_\beta - Q_{\beta gh}^o P_g P_h) - \frac{1}{2} C_{\alpha\beta}^o Q_{\alpha ef}^o Q_{\beta gh}^o P_e P_f P_g P_h. \quad (5)$$

The tensor Q is given by

$$Q_{\alpha bc} = (C^o)_{\alpha\beta}^{-1} q_{\beta bc}^o. \quad (6)$$

Experimental works determine Q directly, rather than q . We can absorb the leftover part of (5) into V^o , giving the effective potential

$$\tilde{V}^o(P) = V^o(P) - \frac{1}{2} C_{\alpha\beta}^o Q_{\alpha ef}^o Q_{\beta gh}^o P_e P_f P_g P_h. \quad (7)$$

Note that the effective potential \tilde{V}^o only differs from V^o in its quartic dependence on P .

First, consider the global minima of the free energy (P^V, ϵ^V). In what follows we will refer to these homogeneous states as *vacua*. The system has multiple vacua, which satisfy

$$\left. \frac{\partial \tilde{V}^o}{\partial P_a} \right|_{P=P^V} = 0, \quad \epsilon_\alpha^V = Q_{\alpha bc}^o P_b^V P_c^V. \quad (8)$$

In this paper, we focus on domain walls: configurations which connect two vacua in physical space and only vary in one direction. To take advantage of this, we will now change coordinates to $(s, \mathbf{t}, \mathbf{r})$, with s in the direction of the wall normal. The rotation matrix is given by

$$R = (s, \mathbf{t}, \mathbf{r})^T \quad (9)$$

We take the important coordinate s , the wall normal, as the *first* basis vector in our new coordinates. Since we are using tensor notation, the material constants transform in a simple way. For example,

$$A_{abcd}^o \rightarrow A_{abcd} = R_{ae} R_{bf} R_{cg} R_{dh} A_{efgh}^o. \quad (10)$$

This transformation also applies to C_{abcd} but not $C_{\alpha\beta}$. As such, we apply the rotation in the ‘‘abcd’’ coordinates and then transform to Voigt notation using (2). We denote the material constants in these new coordinates without any superscript. Note that the material constants depend on the orientation of the wall.

Since the fields only vary in the s direction the compatibility condition (1) simplifies significantly: ϵ_2, ϵ_3 , and ϵ_4 must be constant along the wall (ϵ_1 is special, as the wall-normal s is in the ‘‘1’’ direction in our new coordinate).

We will consider infinite domain walls, which should have finite energy. Hence the vacuum conditions (8) must be satisfied at both ends of the wall.

Suppose the domain wall connects two vacua $P^{V-\infty}$ and $P^{V\infty}$. The strain is fixed at $-\infty$ as

$$\epsilon_\alpha^{V-\infty} = Q_{\alpha bc} P_b^{V-\infty} P_c^{V-\infty}. \quad (11)$$

Now the tensors have no ‘‘o’’ superscript as we have rotated into the new basis. Similarly, the strain at $+\infty$ is given by

$$\epsilon_\alpha^{V\infty} = Q_{\alpha bc} P_b^{V\infty} P_c^{V\infty}. \quad (12)$$

However, the elastic compatibility condition means that the strains perpendicular to the wall are constant, so that $\epsilon_{2/3/4} = \epsilon_{2/3/4}^V$. In particular, these strains at either end of the wall must be equal:

$$Q_{\alpha bc} P_b^{V-\infty} P_c^{V-\infty} = Q_{\alpha bc} P_b^{V\infty} P_c^{V\infty}, \quad \alpha = 2, 3, 4. \quad (13)$$

Note that Q is a function of wall orientation. We'll think of this equation as follows: given ingoing and outgoing vacua, which wall orientations satisfy (13) and hence give a permissible wall? We will see an example in the next section.

Now, given the in and out polarizations and a permissible wall, we would like to minimize the free energy. This would be simple if we could set $\epsilon(s)_\alpha = Q_{\alpha bc} P_b(s) P_c(s)$. Then the potential energy would be \tilde{V} . However, the elastic compatibility condition means that some of the ϵ must be constant, so cannot depend on P in this way. Instead, we first minimize for the constant strains $\epsilon_{2/3/4}$. To help,

we split C and q into parts parallel and perpendicular to the wall

$$q_{abc} = q_{abc}^{\parallel} + q_{abc}^{\perp}, \quad (14)$$

$$C_{\alpha\beta} = C_{\alpha\beta}^{\parallel} + C_{\alpha\beta}^{\perp} + C_{\alpha\beta}^m, \quad (15)$$

where q_{abc}^{\perp} is only nonzero when $\alpha = 2, 3, 4$, q_{abc}^{\parallel} is nonzero when $\alpha = 1, 5, 6$, $C_{\alpha\beta}^{\perp}$ is nonzero when α and β both belong to $\{2, 3, 4\}$; C^{\parallel} is only nonzero when both belong to $\{1, 5, 6\}$; and C^m is nonzero otherwise. As seen earlier, the perpendicular strains satisfy

$$\epsilon_{\alpha} = \epsilon_{\alpha}^V = Q_{abc} P_b^{V\infty} P_c^{V\infty}, \quad \alpha = 2, 3, 4. \quad (16)$$

The parallel strains are free to minimize the part of the energy which depends on them,

$$\frac{1}{2} C_{\alpha\beta}^{\parallel} \epsilon_{\alpha} \epsilon_{\beta} + C_{\alpha\beta}^m \epsilon_{\alpha} \epsilon_{\beta}^V - q_{abc}^{\parallel} \epsilon_{\alpha} P_b P_c, \quad (17)$$

which is minimal when

$$\epsilon_{\alpha} = (C^{\parallel})_{\alpha\beta}^{-1} (q_{\beta bc}^{\parallel} P_b P_c - C_{\beta\gamma}^m \epsilon_{\gamma}^V). \quad (18)$$

Here the inverse of C^{\parallel} is defined as the inverse of the 3×3 nonzero part, projected back into its 6×6 form. This is the unique matrix which satisfies

$$(C^{\parallel} (C^{\parallel})^{-1})_{\alpha\beta} = \begin{cases} \delta_{\alpha\beta} & \alpha = 1, 5, 6 \\ 0 & \text{otherwise} \end{cases}. \quad (19)$$

We can make more sense of Eq. (18) using the fact that $q^{\parallel} = C^{\parallel} Q^{\parallel} + C^m Q^{\perp}$. Then

$$\epsilon_{\alpha} = Q_{abc}^{\parallel} P_b P_c + (C^{\parallel})_{\alpha\beta}^{-1} C_{\beta\gamma}^m (Q_{\gamma bc}^{\perp} P_b P_c - \epsilon_{\gamma}^V) \quad (20)$$

for $\alpha = 1, 5, 6$. As $s \rightarrow \pm\infty$, the second term vanishes and these strains also approach their vacuum values (8), as we would expect.

Overall, the minimal energy strains are given by

$$\epsilon_{\alpha} = H_{\alpha bc} P_b P_c + K_{\alpha}, \quad (21)$$

where

$$H_{\alpha bc} = \begin{cases} Q_{abc}^{\parallel} + (C^{\parallel})_{\alpha\beta}^{-1} C_{\beta\gamma}^m Q_{\gamma bc}^{\perp} & \alpha = 1, 5, 6 \\ 0 & \alpha = 2, 3, 4 \end{cases}; \quad (22)$$

$$K_{\alpha} = \begin{cases} -(C^{\parallel})_{\alpha\beta}^{-1} C_{\beta\gamma}^m \epsilon_{\gamma}^V & \alpha = 1, 5, 6 \\ \epsilon_{\alpha}^V & \alpha = 2, 3, 4 \end{cases}. \quad (23)$$

Finally, we substitute these expressions into the free energy to find an effective free energy for P , which depends on a single coordinate s . It is

$$F = \frac{1}{2} G_{sasb} \partial_s P_a \partial_s P_b + V(P) \quad (24)$$

$$V = \tilde{A}_0 + \tilde{A}_{ab} P_a P_b + \tilde{A}_{abcd} P_a P_b + A_{abcdef} P_a P_b P_c P_d P_e P_f \quad (25)$$

with

$$\begin{aligned} \tilde{A}_0 &= \frac{1}{2} K_{\alpha} K_{\beta} C_{\alpha\beta}, \\ \tilde{A}_{ab} &= A_{ab} + \frac{1}{2} (C_{\alpha\beta} H_{\beta ab} + C_{\beta\alpha} H_{\alpha ab} - 2q_{\alpha ab}) K_{\alpha}, \\ \tilde{A}_{abcd} &= A_{abcd} + \frac{1}{2} (H_{\beta ab} C_{\beta\alpha} - 2q_{\alpha ab}) H_{\alpha cd}. \end{aligned}$$

This result is the general form of the free energy for any wall orientation. After some algebra, we can compare our results to the set of special cases considered in Ref. [25], and they match. The key advantage of our formalism is that there is a reasonably simple chain from the material coefficients A , C , and Q to the effective model for a given vacuum and wall orientation (24). The final analytic expressions for \tilde{A} are incredibly complicated, especially when we allow for arbitrary walls. Hence, when writing code to solve the problem, we do not deal with them directly. Instead, we start with A , C , and Q and implement the results of this section.

Having dealt with the geometry of the system, one could now include electrostatic effects. In Ref. [13], it was considered that a perfectly insulated ferroelectric has an electrostatic penalty proportional to $(P_s - P_s^V)^2$. A consequence of this fact is that low-energy walls are always orthogonal to the Néel component of the vacuum polarization (note that the Néel component is the component in the wall-normal direction s). Walls which satisfy this constraint are called ‘‘neutral’’ walls. We will neglect this effect and consider our model system of walls in arbitrary orientations. Provided they are neutral, similar walls may exist in real systems but with a reduced Néel component due to the quadratic term discussed in this paragraph. Hence we will often focus on neutral walls in our results.

Let us now consider symmetry. The initial potential V^o is symmetric under all elements of the symmetry group of the lattice. In our example, this is the cubic group. But the final potential and the tensors \tilde{A} are not totally symmetric, since we have chosen a special direction (the wall-normal s) and the polarization vacuum value at both ends of the wall, $P^{V\infty}$ and $P^{V-\infty}$. The vectors s , $P^{V\pm\infty}$ define lines, and we can mark points on a cube where these lines intersect it. The symmetry of the problem is equal to the symmetry of the marked cube. For example, consider the wall along $s = (0, 0, 1)$ joining $P^V \propto (1, 1, 1)$ to $-P^V$. The corresponding potential will be invariant under π rotations about $(1, -1, 0)$, a rotation by π about $(0, 0, 1)$ combined with a reflection about the $z = 0$ plane, and combinations of these. Overall, a $C_2 \times C_2$ subgroup of O_h .

Although somewhat obscured by the notation, the potential V is a polynomial of order 6 and so domain walls in ferroelectrics are described by a multicomponent ϕ^6 theory. This theory, originally proposed in Ref. [26], has been widely studied owing to its highly nontrivial ‘‘fractal’’ dynamics between domain walls [27,28]. Multicomponent theories have been shown to exhibit even more complex dynamics [29]. Unfortunately, the dynamics governing DWs in ferroelectrics are first order, so these studies are not directly applicable to ferroelectric dynamics.

III. STATIC WALLS

For the rest of the paper, we will consider a specific ferroelectric, barium titanate with perfect screening. The material constants are given in Appendix. The system has cubic symmetry and there are four phases with different global minima. These are

(i) $T < 201$ K, the rhombohedral phase, with $P^V = (p^r, p^r, p^r)$ plus permutations;

TABLE I. The allowed walls in a defect-free ferroelectric. We take the temperature to be 150, 250, and 300 K for the rhombohedral, orthorhombic, and tetragonal phases, respectively. The energy is in dimensionless units; it can be converted to Joules through the factor $\sqrt{G_{11}^3(P^V)^4/A_{11}}$.

Name	$P^{V-\infty}$	$P^{V\infty}$	Wall (s)	Energy
R71°	(p, p, p)	$(-p, p, p)$	(1,0,0) (0,1,1)	0.509 0.117
R107°	(p, p, p)	$(-p, -p, p)$	(1,1,0) (0,0,1)	0.536 0.240
R180°	(p, p, p)	$(-p, -p, -p)$	All allowed	
O60°	$(p, p, 0)$	$(p, 0, p)$	(0, -1, 1)	0.193
O90°	$(p, p, 0)$	$(p, -p, 0)$	(1,0,0) (0,1,0)	0.232 0.992
O120°	$(p, p, 0)$	$(0, -p, p)$	(1,0,1)	0.435
O180°	$(p, p, 0)$	$(-p, -p, 0)$	All allowed	
T90°	$(p, 0, 0)$	$(0, p, 0)$	(1,1,0) (1, -1, 0)	0.405 0.405
T180°	$(p, 0, 0)$	$(-p, 0, 0)$	All allowed	

(ii) $201 \text{ K} < T < 282 \text{ K}$, the orthorhombic phase, with $P^V = (p^o, p^o, 0)$ plus permutations;

(iii) $282 \text{ K} < T < 400 \text{ K}$, the tetragonal phase, with $P^V = (p^t, 0, 0)$ plus permutations;

(iv) $400 \text{ K} < T$, the spherical phase, with $P^V = (0, 0, 0)$.

The permutations are any symmetry elements of the cubic group. So there are 8, 12, and 6 vacua for the rhombohedral, orthorhombic, and tetragonal phases. Throughout this work we choose $T = 150, 250,$ and 300 K as representative temperatures of each nontrivial phase. The vacuum values p^i can be calculated analytically using (8), but the expressions are unpleasant.

The allowed walls satisfy (13), which we consider to be an equation in terms of the wall-normal s through

$$Q_{abcd} = R(s)_{ae}R(s)_{bf}R(s)_{cg}R(s)_{dh}Q_{efgh}^o. \quad (26)$$

The allowed combinations of $P^{V-\infty}$, $P^{V\infty}$, and s are displayed in Table I. The wall names are given by the angle between the connected vacua. We see that (13) is quite restrictive and only some walls are allowed.

We now find minimal energy domain walls for a given pair of vacua and wall orientation. We first consider those vacua with a discrete set of allowed walls: the R71°, R107°, O60°, O90°, O120°, and T90° walls. The first task is to find appropriate initial data. We expect the wall, which connects two minima, to pass through (or near) a saddle point or maxima of the potential. We can classify all such points and label them as P^{VA} . Then we create initial data which looks like a wall linking $P^{V-\infty}$ and $P^{V\infty}$ through P^{VA} , such as

$$\frac{1}{2}(1 - \tanh(s))P^{V-\infty} + \frac{1}{2}(1 + \tanh(s))P^{V\infty} + \text{sech}(s)P^{VA}. \quad (27)$$

We then flow these initial data using the arrested Newton flow method, with fixed boundary data. The idea, originally proposed in Ref. [30], is to replace the first-order gradient flow with second-order time dynamics

$$\ddot{P}_a = -\frac{\delta F}{\delta P_a}, \quad P(-\infty) = P^{V-\infty}, \quad P(\infty) = P^{V\infty}. \quad (28)$$

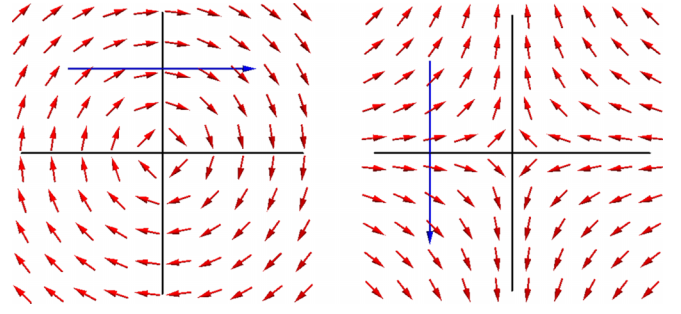


FIG. 1. Two possible 2D structures. We can think of the vortex (left) as made from low-energy head-to-tail walls (e.g., along the wall-normal highlighted in blue) connecting the regions separated by black lines. The antivortex (right) is made from high energy head-to-head and tail-to-tail walls. Our analysis of domain wall energies suggest that the vortex will have lower energy.

The initial configuration will accelerate towards an energy minimum but, without interference, will not stop there. We interfere by checking the energy of the configuration at each time step and only proceed if the energy falls. If the energy increases, we set the field velocity to zero and restart the time evolution. Again the field will move towards a minima. Once the variation is below some critical values, we are close to a solution to the equations of motion: either a minimizer or a saddle point. We then add random noise to the simulation, which destabilizes the configuration if it is a saddle point. Once a configuration is stable to random fluctuations, we are confident that it is a local minimizer. Arrested Newton flow is much faster than standard gradient flow, as the second-order dynamics allow for much larger time steps.

We repeat this process for many initial configurations, including ones which pass through each possible P^{VA} and save the result with lowest energy. The energies of these configurations are written in Table I. We have switched to dimensionless units by dividing P by $|P^V|$, the A s by A_{11} and the G s by G_{11} . The length and energy units are then given by $\sqrt{G_{11}/A_{11}}$ and $\sqrt{G_{11}^3(P^V)^4/A_{11}}$. Note that these units depend on temperature.

Certain wall directions, connecting the same vacua, are energetically preferred. For instance, O90° walls between $(p^o, p^o, 0)$ and $(p^o, -p^o, 0)$ in the (1,0,0) direction are preferred over those in the (0,1,0) direction. This confirms the result of Ref. [31], that head-to-tail walls are preferred over head-to-head and tail-to-tail walls. The reason is that the “derivative” energy, $G_{sash}\partial_s P_a \partial_b P_b / 2$, of the head-to-tail wall is proportional to G_{44} , which is much smaller than of the head-to-head wall, which is proportional to G_{11} .

That certain wall directions have lower energy has implications for higher-dimensional objects. Consider the two 2D configurations in Fig. 1. The first, a vortex, should be energetically preferred to the second, an antivortex, because it is constructed from walls with lower energy. This explains why the Ising lines from Ref. [32] have a preferred (positive) chirality.

IV. STATIC 180° WALLS

Unlike the walls in the previous section, the 180° walls are allowed to be in any orientation. For a given wall orientation,

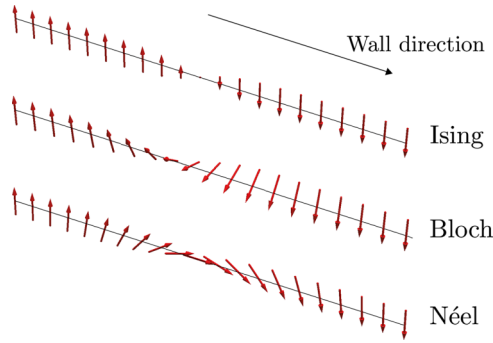


FIG. 2. The three prototypical domain walls.

the most important question is: is the wall Ising, Bloch or Néel? An Ising wall has only one polarization component, which must be proportional to the ground state \mathbf{P}^V . A Néel wall additionally has nonzero polarization in the direction of the wall-normal, while a Bloch walls can vary perpendicularly to the wall-normal. The three types are shown in Fig. 2. Pure Bloch (with zero Néel component) and pure Néel (with zero Bloch component) walls are only allowed when the wall normal \mathbf{s} is orthogonal to the ground state polarization \mathbf{P}^V , which is often the case [3]. However, even when this is not the case, we can define the Ising, Néel and Bloch components of the polarization vector as

$$\mathbf{P}(s) = P_I(s)\hat{\mathbf{P}}^V + P_N(s)\tilde{\mathbf{s}} + P_B(s)\hat{\mathbf{P}}^V \times \tilde{\mathbf{s}}, \quad (29)$$

where $\tilde{\mathbf{s}}$ is the linear combination of \mathbf{P}^V and \mathbf{s} which is orthogonal to \mathbf{P}^V . For neutral walls, \mathbf{P}^V and \mathbf{s} are automatically orthogonal. In this case, $\tilde{\mathbf{s}}$ is simply equal to \mathbf{s} and our definitions of Ising, Bloch, and Néel components are the same as those used in Ref. [3]. But even for a generic wall the components P_I , P_B , and P_N tell us which type of basic wall it is closest to. The deconstruction (29) is only allowed if \mathbf{P}^V and \mathbf{s} are not equal.

The rarest wall type is Bloch. Hence, we will search for a Bloch wall when varying the wall orientation. We can gain some insight by looking at the potential energy (24) at the center of the wall, when $P_I = 0$. That is, we look at the energy

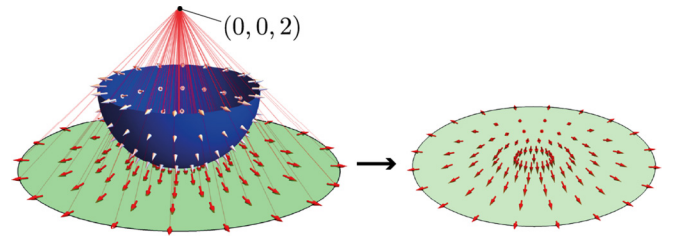
$$V(P_N, P_B) = V(\mathbf{P} = P_N\tilde{\mathbf{s}} + P_B\hat{\mathbf{P}}^V \times \tilde{\mathbf{s}}). \quad (30)$$

This is a sextic polynomial in two variables whose coefficients depend nontrivially on the wall orientation (as explained in Sec. II). Hence we can classify its stationary points semi-analytically. A minimum at $(P_N, P_B) = (0, p_b)$ suggests that the system could support a Bloch wall while a minimum at $(P_N, P_B) = (p_n, 0)$ suggests there could be a Néel wall. Of course, the derivative energy is also important, but this potential provides a theoretical starting point.

We now search for wall orientations which support interesting walls and study them. To do so, let us change to coordinates which reflect the choice of wall orientation through the angles θ and ϕ :

$$\mathbf{s} = (\cos(\theta), \sin(\theta)\sin(\phi), \sin(\theta)\cos(\phi)), \quad (31)$$

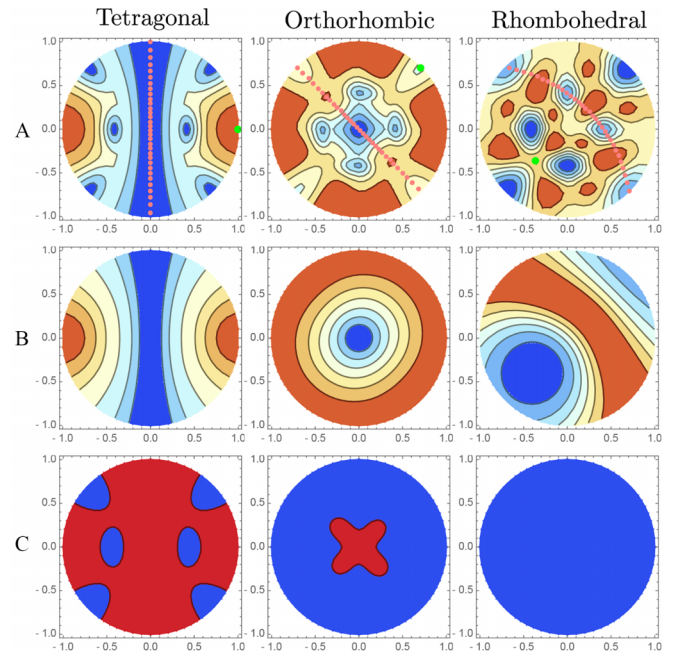
$$\mathbf{r} = (\sin(\theta), -\cos(\theta)\sin(\phi), -\cos(\theta)\cos(\phi)). \quad (32)$$


 FIG. 3. A visualization of the projection map used in Fig. 4. We take a sphere whose normal vector are the wall-normals \mathbf{s} (white arrows, left) and project these from $(0,0,2)$ to a disk on the plane $z = 0$ (right).

To begin, we find the overall energy minimizer for the given wall orientation following the procedure described in the previous section for non- 180° walls. We also find the minimal energy Ising wall by demanding that

$$\mathbf{P}(s) \cdot \tilde{\mathbf{s}} = \mathbf{P}(s) \cdot (\mathbf{P}^V \times \tilde{\mathbf{s}}) = 0. \quad (33)$$

This condition is easy to implement numerically through a projection, and means that the polarization vector has only one component: proportional to the ground state. We do this calculation to check when non-Ising walls are favoured over Ising walls. These results are shown in Fig. 4. We plot the energy of the energy-minimizing wall in row A and the energy


 FIG. 4. Plot of the wall-energy as a function of wall-normal \mathbf{s} . Each point on each disk corresponds to a different unit wall-normal, with the mapping show in Fig. 3. Red and blue represents large and small energies, respectively. The minimal energy wall (row A), minimal energy wall subject to the Ising condition $\mathbf{P}(0) = \mathbf{0}$ (row B) and difference between the energies (row C) are shown. The red regions contains wall-directions where the non-Ising wall has at least 10% less energy. The tetragonal, orthorhombic and rhombohedral walls are between the vectors $(p', 0, 0)$ to $(-p', 0, 0)$, $(p^\circ, p^\circ, 0)$ to $(-p^\circ, -p^\circ, 0)$ and (p', p', p') to $(-p', -p', -p')$, shown as a green dot in row A, at temperatures 300, 250, and 150 K, respectively.

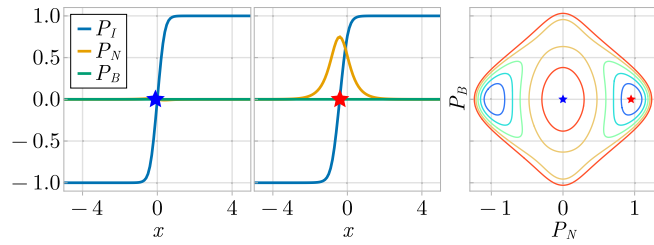


FIG. 5. The Ising wall (left), minimal energy Néel wall (middle) and a contour plot of the potential energy (30) for $T = 300$ K, $\mathbf{P}^V = (p^r, 0, 0)$, and $\mathbf{s} = (1/\sqrt{2}, 1/2, 1/2)$. The center point of each wall is marked with a star. The Ising, Bloch, and Néel components of the wall, defined in 30 are plotted in blue, orange, and green, respectively. Neutral wall orientations are highlighted by a pink line.

of the energy-minimizing Ising wall in row B. In row C the blue region represents where the non-Ising wall has 10% lower energy than the Ising wall. Here, the wall orientation is parameterized using a Riemann half-sphere projected onto a disk in the plane. The projection is displayed graphically in Fig. 3. The final disk is rescaled to have unit radius. We highlight the neutral wall orientation, where $\mathbf{P}^V \cdot \mathbf{s} = 0$, as a pink line in Fig. 4. In total, we found the energy minimizing domain wall for 30 000 different combinations of wall orientations and initial conditions.

For a given (θ, ϕ) pair, we can find the minima of the potential (30). If this analysis suggests there could be a Bloch or Néel wall, we study the example in more detail. This is how we have found the examples discussed in the remainder of this section.

In the tetragonal phase (left column of Fig. 4), the wall connects vacua pointing towards cube faces: we take $(p^r, 0, 0)$ and $(-p^r, 0, 0)$. For Ising walls, the energy only depends on the angle between the wall and vacua, and the energy is minimized when the wall is perpendicular to the vacuum states. Non-Ising DWs are preferred in several orientations. An interesting example is for the charged wall with $\mathbf{s} = (1/\sqrt{2}, 1/2, 1/2)$. The potential energy at the center of the wall (30) for this orientation is plotted in Fig. 5 (middle) and suggests there could be a Bloch or Néel wall, since there are minima along these axes. It costs less potential energy to pass through a minima of the potential at the wall-center but it costs gradient energy to move the polarization away from $(P_N, P_B) = (0, 0)$. In this case, the Néel wall has lowest energy: the cost of gradient energy to pass through the Néel point is lower than the potential energy saved. However, there does exist a higher energy, locally minimal, Ising wall. This example highlights the utility of the potential energy plots as they can predict which walls may have low energy and the importance of fitting the gradient coefficients G correctly. If G was larger, it would cost more energy to create the Néel wall and thus it could be disfavoured compared to the Ising wall.

In the orthorhombic phase, our DWs connect the vacua $(p^o, p^o, 0)$ and $(-p^o, -p^o, 0)$. By examining Fig. 2, we see that the lowest energy orientations are on the points of a diamond with, e.g., $\mathbf{s} = (0, 1, 1)/\sqrt{2}$. Non-Ising walls are preferred almost everywhere, though near $\mathbf{s} = (0, 0, 1)$ the Ising

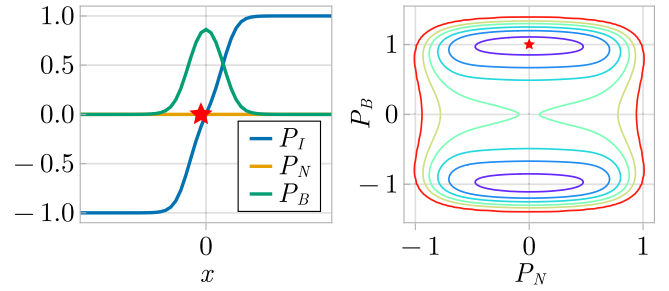


FIG. 6. The minimal energy $90^\circ - 90^\circ$ neutral wall for $T = 250$ K, $\mathbf{P}^V = (p^o, p^o, 0)$, and $\mathbf{s} = (0, 0, 1)$ (left) and a contour plot of the potential energy (right).

walls have similar energies. Usually the non-Ising walls look like pairs of smaller degree walls. For example, consider the neutral wall with $\mathbf{s} = (0, 0, 1)$ the potential energy suggests that there is a possible Bloch wall. When constructed, the wall looks like two overlapping 90° walls, one joining $(1, 1, 0)$ to $(1, -1, 0)$ and another from $(1, -1, 0)$ to $(-1, -1, 0)$. The potential and solution can be seen in Fig. 6.

Finally in the rhombohedral phase, the domain walls connect (p^r, p^r, p^r) and $(-p^r, -p^r, -p^r)$. The energy of the minimizing walls is a complicated pattern depending heavily on the wall orientation. Part of this has been seen before for neutral walls in Ref. [7]. The energy minimizing walls have one zero component of \mathbf{s} , such as $\mathbf{s} = (1, 1, 0)/\sqrt{2}$. Non-Ising walls are preferred in all orientations, and some of these have been discovered previously [2]. In this phase, we do find Bloch wall solutions, although they are not energy-minimizing and are charged. One example is shown in Fig. 7. The potential energy has minima in six places: two Bloch points and four mixed points which together form an approximate hexagon. The mixed points have lower energy than the Bloch points. We plot a nonminimizing solution which passes near the Bloch point (middle). Note that these are not pure Bloch walls, but the Bloch component is large compared to the Néel component. We also plot the solution which passes near the mixed point (left) and this has lower energy. It passes near vacua which lie on the corners of the cube. In real barium titanate, only neutral walls can be stable. Hence we plot the minimal energy neutral wall in Fig. 8. This looks like three consecutive overlapping

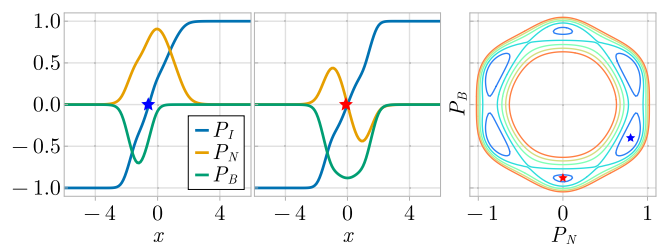


FIG. 7. The minimal energy mixed wall (left) and higher energy Bloch wall (middle) in the rhombohedral phase at $T = 150$ K and $\mathbf{s} = (1/\sqrt{2}, -1/2, -1/2)$. The potential energy for the wall-center (middle); the mixed wall passes close to the point $(P_N, P_B) \approx (0.8, -0.4)$ while the Bloch wall passes close to the point $(P_N, P_B) \approx (0, -0.9)$.

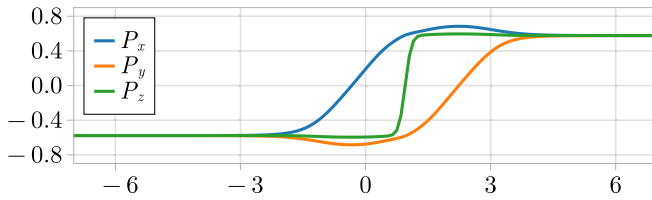


FIG. 8. The minimal energy neutral wall in the rhombohedral phase at $T = 150$ K, with $s = (1/\sqrt{2}, -1/\sqrt{2}, 0)$. It takes the form of three consecutive short walls which overlap.

71° walls, similar to the orthorhombic walls which looks like two short 90° walls.

Overall, we have found a variety of domain wall solutions. The minima of the potential energy (30) can suggest where certain types of walls can form, but their existence and energy depend on various factors including the depth of the minima and the size of the derivative energy. There are non-Ising walls preferred in every phase of the system.

V. ASYMPTOTICS AND INTERACTIONS

We will now calculate the asymptotic form of a domain wall, and use this to understand their interaction. This will allow us study wall-wall pairs and show that, in general, Ising-Ising walls are unstable to collapse but other pairs may not be.

Consider the tail of a wall, where

$$\mathbf{P} = \mathbf{P}^V + \mathbf{p} \quad (34)$$

and p_a is small. The Euler-Lagrange equations for the tail are

$$-G_{sasb} \partial_s^2 p_b + \left. \frac{\partial^2 V}{\partial P_a \partial P_b} \right|_{P^V} p_b = 0, \quad (35)$$

which has solution

$$\mathbf{p} = \sum_i \boldsymbol{\mu}_i e^{-\lambda_i s}, \quad (36)$$

where λ_i^2 and $\boldsymbol{\mu}_i$ are the eigenvalues and eigenvectors of

$$G_{sasc}^{-1} \left. \frac{\partial^2 V}{\partial P_c \partial P_b} \right|_{P^V}. \quad (37)$$

The leading behavior is described by the eigenvector with the smallest eigenvalue.

Now consider two walls, one going from $\mathbf{P}^{V-\infty}$ to \mathbf{P}^{V_0} and another from \mathbf{P}^{V_0} to $\mathbf{P}^{V\infty}$. Suppose the walls have positions $\mp X$ with $|X| \gg 1$ and denote them $\mathbf{P}^{\mp X}$. Near the central vacuum, the walls take the form $\mathbf{P}^{\mp X}(s) = \mathbf{P}^{V_0} + \mathbf{p}^{\mp X}(s)$. We can approximate the combined wall as

$$\mathbf{P}(s) = \mathbf{P}^{-X}(s) + \mathbf{P}^X(s) - \mathbf{P}^{V_0} \quad (38)$$

$$\approx \begin{cases} \mathbf{P}^{-X}(s) + \mathbf{P}^X(s) - \mathbf{P}^{V_0} & \text{for } s < 0 \\ \mathbf{P}^{-X}(s) + \mathbf{P}^X(s) - \mathbf{P}^{V_0} & \text{for } s > 0 \end{cases}. \quad (39)$$

Using this approximation, we can evaluate the energy of the configuration as a series in \mathbf{p} . The calculation is done in detail in Ref. [33], and the result only depends on the tails:

$$E(\mathbf{p})^{\text{int}} = G_{sasb} (p_b^X \partial_s p_a^{-X} - p_b^{-X} \partial_s p_a^X). \quad (40)$$

This simple expressions tells us if the walls attract or repel based solely on their tails. In fact, there is a simple graphically

interpretation. If the tails come together to form a saddle point, they repel. If they form a maximum or minimum, they attract.

First, consider two ‘‘short’’ walls which combine to make long wall, like the two 90° walls seen in Fig. 6 (center). Here, the wall tails in the Bloch component P_B come together to form a maximum, while the walls in the Ising component P_I form a saddle point. Hence the Bloch components create an attractive force, while the Ising components create a repulsive force. Which is dominant depends on the slope of the walls and the eigenvalues of (37). In this case, at $T = 250$ K, the attractive force wins.

For a simpler example which we can do in more detail, consider two 180° Ising walls: the first connecting a vacuum \mathbf{P}^V to its negative $-\mathbf{P}^V$ and the second $-\mathbf{P}^V$ back to \mathbf{P}^V . For simplicity, we will consider an explicit example. Choose coordinates (s, \mathbf{r}, t) so that the wall-normal is s and the connected vacua are in the \mathbf{r} direction so that $\mathbf{P}^{V\infty} = (0, P^V, 0)$. The wall tails at $s = 0$ are given by

$$\mathbf{p}^{-X} = b\hat{\mathbf{r}} \exp(-\lambda(s+X)), \quad \mathbf{p}^X = b\hat{\mathbf{r}} \exp(\lambda(s-X)), \quad (41)$$

where

$$\lambda^2 = G_{sr sr}^{-1} \left. \frac{\partial^2 V}{\partial P_r \partial P_r} \right|_{-P^V}. \quad (42)$$

Note that, since $-\mathbf{P}^V$ is a vacuum, the Hessian is positive. Using (40), we find

$$E^{\text{int}} = -2b^2 \lambda G_{sr sr} \exp(-2\lambda X). \quad (43)$$

The eigenvalue and $G_{sr sr}$ are positive and so the energy is negative. The walls can decrease the energy by decreasing X and so the walls attract and will, eventually, annihilate. This result is well known in kink models: kinks and antikinks always attract in one-component theories. The Ising wall ansatz reduces our multicomponent theory to a single component one.

Domain wall clusters

As we have seen, there can be walls which attract in one component and repel in another. We can use this fact to try and construct stable wall clusters, and use the asymptotic analysis to search for wall orientations which support long-range attraction. We then evolved the system to see if there are stable solutions.

One example with stable domain wall clusters is the configuration joining $\mathbf{P}^V = p^o(1, 1, 0)$ to $-\mathbf{P}^V$ and back again along the wall with $s = (1, 1, 1)/\sqrt{3}$. This has dominant eigenvector $(0, 0, 1)$ and the wall tails in this channel create an attractive force at long range. The second most dominant eigenmode creates a repulsion. The balance between the attraction and repulsion in different eigenchannels generates the conditions for stable configurations. (The stable configuration for this wall is shown in Fig. 9.) Note that the final configuration traces a loop around the equator in target space. For the walls to collapse, this loop must contract. But this costs significant energy because both the point $\mathbf{P} = \mathbf{0}$ and the lines $P_z \neq 0$ have high energy. This energy barrier stops the loop from becoming a point, and hence the system is stable. Unfortunately, since the wall is charged, it is unlikely to be stable in barium titanate. A cluster along $s = (0, 0, 1)$, constructed from walls of the type seen in Fig. 6 would be neutral and could be stable.

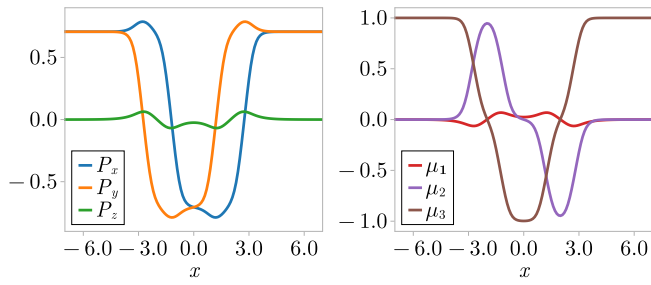


FIG. 9. A configuration with long-range attraction but short-range repulsion, allowing for a stable local minimum. We plot the field in xyz components and in the asymptotic eigenbasis. There is attraction in the first and third eigencomponents and repulsion in the second.

Both unstable and stable wall-wall pairs can be constructed for the same wall orientation and phase. We construct initial data based on two Ising wall and two non-Ising walls in the top of Fig. 10. We create the Ising walls by demanding that the field vanishes at two points. We then remove this constraint and flow the field. The time evolution is read from top to bottom. As predicted by the asymptotic analysis, the Ising walls annihilate while the non-Ising walls stabilize.

Generally, it is rare to find wall orientations which support long-range attraction for the wall pairs. However, there are many examples, especially in the rhombohedral phase, where

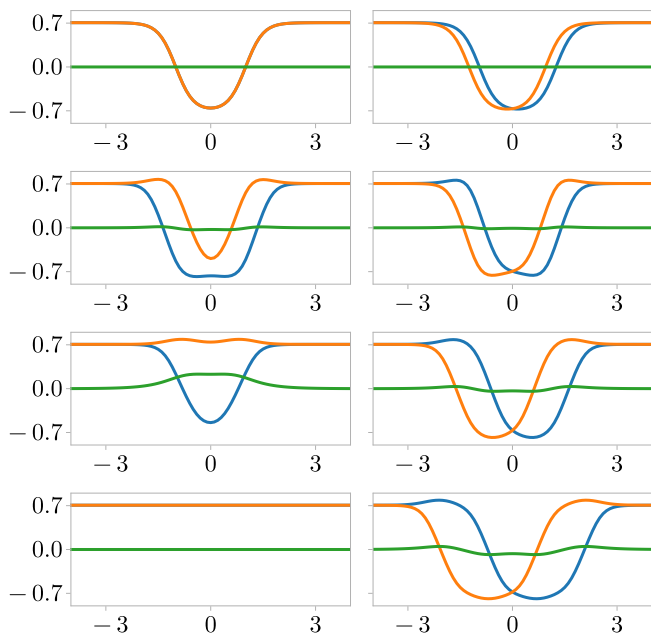


FIG. 10. Gradient flow applied to initial data representing Ising-Ising and non-Ising pairs in the orthorhombic phase at $T = 200$ K, for the wall-normal $s = (1, 1, 1)/\sqrt{3}$ and boundary polarization $\mathbf{P}^\infty = (p^\rho, p^\rho, 0)$. We plot the xyz components of the polarization vector, coloured in the same way as in Fig. 9. Time is read from top to bottom. The Ising-Ising pair attract and annihilate into the vacuum while the non-Ising walls fall into a stable minima.

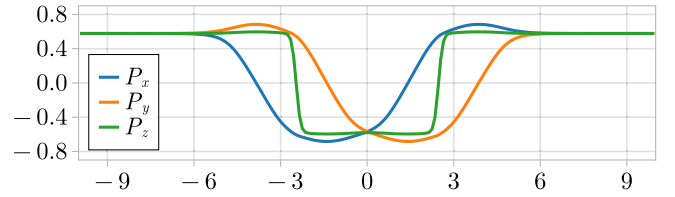


FIG. 11. A stable wall-wall pair in the rhombohedral phase at $T = 150$ K. Here, $s = (1, -1, 0)/\sqrt{2}$. The order of the components is vital for ensuring the stability of this configuration.

the different eigenmodes give separately attractive and repulsive interactions. In these situations it is possible that there are stable minima, such as the configuration in Fig. 11, due to nonlinear effects. This wall is neutral, so is possibly stable in real barium titanate. To check this, one should include electrostatic effects as for example was discussed in Ref. [7,13]. The long-range attraction is required to prove analytically that these are truly minima. For the other walls we can numerically show that they are stable by calculating the Hessian around the configuration. We have done this for the field shown in Fig. 11.

We can also look for longer clusters of domain walls but adjusting the initial conditions for the gradient flow. For example, a stable 6-cluster is displayed in Fig. 12.

An important application of Bloch walls are their potential use in high-density memory storage. An appealing aspect is that Bloch walls can have two, or more, energetically equivalent ground states. Hence one can have a memory cell with more than one bit of information in it, and these can be switched using an electric field. Such a bistable Bloch wall was studied in Ref. [34]. A domain wall cluster contains as many states as a bistable Bloch wall. This is because the stability of the cluster depends on the intertwining of the polarization components, as seen in Fig. 11 where the P_y and P_x components take turns crossing the axis. There is another cluster, where the P_x and P_y components are swapped, but no others. Hence there are two energetically equivalent clusters, the same number as there are energetically equivalent Bloch walls in Ref. [34].

VI. LINEAR AND NONLINEAR STABILITY

Given a solution to the static equations of motion $\mathbf{P}^0(s)$, we can study its linear stability through its normal modes, $e_a(s)$.

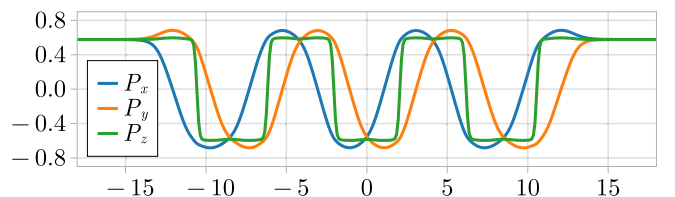


FIG. 12. A neutral stable cluster formed of six domain walls. Here, $T = 150$ K and $s = (1, -1, 0)/\sqrt{2}$.

These satisfy

$$\hat{H}[P^0(s)]_{ab}e_b = \omega^2 e_a, \quad (44)$$

where \hat{H} is given by

$$\hat{H}_{ab} = -G_{sasb}\partial_s\partial_s + \frac{\partial^2 V}{\partial P_a \partial P_b} \Big|_{P^0(s)}. \quad (45)$$

This is a Schrödinger type equation and methods to find its solutions are well known. We do so using a gradient flow method developed in Ref. [35] and applied to higher dimensional system in Ref. [36]. Briefly, we take a random initial perturbation e and evolve it using

$$\partial_\tau e = -\hat{H}e. \quad (46)$$

This has solution

$$e(s) = \sum_n \exp(-\omega_n \tau) e_n(s), \quad (47)$$

where e_n and ω_n are eigenfunctions and eigenvalues. After a long time, the lowest energy mode will dominate the flow while all other modes are exponentially suppressed. We save the lowest mode and repeat the process while projecting out our saved mode. The second lowest frequency mode then dominates the solution at large times and we save this. And so on.

Let us consider an example: the stable wall-wall pair found in the previous section, seen in Fig. 9. Denote the solution $P^W(s)$. It has a \mathbb{Z}_2 reflection symmetry

$$(P_x^W(s), P_y^W(s), P_z^W(s)) = (P_y^W(-s), P_x^W(-s), P_z^W(-s))$$

and so we can label the modes depend on whether they transform trivially under this transformation, or pick up a sign. We find the four lowest frequency normal modes with frequencies and signs $\omega^P = 0.0^-, 0.2^+, 1.34^+,$ and 1.35^- . All modes are positive, confirming that the wall-pair is a local minimum. Physically, the first mode corresponds to translations and hence costs no energy to excite. In the second, the walls oscillate around their positions: moving towards and away from each other. The final two modes are breathing modes: the walls increase and decrease in size, either in- or out-of-phase.

We know that there is a configuration with lower energy than the wall-pair: the vacuum $P(s) = P^V$. Hence, although the configuration is linearly stable, it cannot be stable under large perturbations. We can use the simplified string method to understand the nonlinear stability. This method was originally proposed for chemical reactions [37], but has also been used study stability of topological defects in condensed matter [38]. We construct a ‘‘string’’ of n configurations which interpolate between the wall pair and the vacuum, parameterized by $h_i = \frac{i-1}{n-1} \in [0, 1]$:

$$P(h_i, s) = (1 - h_i)P^W(s) + h_i P^V. \quad (48)$$

We then minimize the energy of the band

$$\sum_{i=1}^n F[P(h_i)], \quad (49)$$

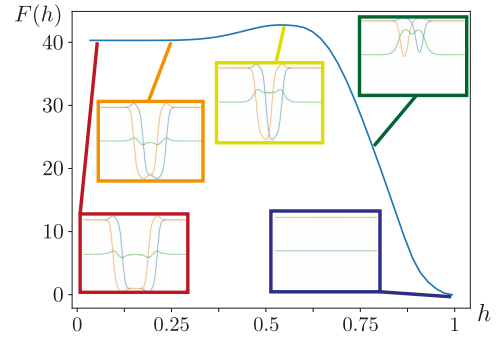


FIG. 13. The energy $F(P(h))$ of our minimized band of configurations as a function of the distance along the string h , joining the minimum $P^W(s)$ to the vacuum P^V for $T = 200$ K. Several configurations along the band are plotted, using the same colouring and axes are used in Fig. 9. The band passes through a local minimum ($h \approx 0.25$), saddle point ($h \approx 0.6$).

using a gradient flow, with the end points fixed as

$$P(0, s) = P^W(s) \quad P(1, s) = P^V. \quad (50)$$

In the simplified string method we demand that, during the flow, the points are evenly spaced on the string. In detail, we define a measure of distance

$$d(P(h_i), P(h_j))^2 = \int (P(h_i) - P(h_j))^2 ds. \quad (51)$$

Then the k th configuration is a distance

$$L_k = \sum_{i=1}^{k-1} d(P(h_i), P(h_{i+1})). \quad (52)$$

along the string, and the total length is given by L_n . After we have flowed for some time, we recalculate the total length of the string and linearly resample the configurations by demanding that the configurations are evenly spaced, at positions $L_n^{\text{new}} = L_n h_i$. If $L_{k-1} < L_n^{\text{new}} < L_k$, then the resampled configuration at that point is given by

$$\frac{L_k - \tilde{L}}{L_k - L_{k-1}} P(h_{k-1}, s) + \frac{\tilde{L} - L_{k-1}}{L_k - L_{k-1}} P(h_k, s). \quad (53)$$

The process generates a low-energy path in configuration space joining two minima which, by Morse theory, is guaranteed to pass through a saddle point. The energy of the saddle point gives the energy barrier to collapse. We apply the simplified string method with end configurations $P^W(s)$ and two widely separated walls. The energy $E(h_i)$ and some configurations $P(h_i, s)$ from these simulations are plotted in Fig. 13.

In the path from P^W to the vacuum, the configuration must either pass through $P = \mathbf{0}$ or contain a nonzero P_z . Both cost significant energy and, in this case, the lower energy option is to increase P_z . On target space, the initial state is a circle while the end state is a point. So, during the process the circle has contracted to a point: the topology of the configuration has changed. The energy barrier exists because changing this

topology costs energy (due to the high energy cost away from the $P_x^2 + P_y^2 = |P^V|^2$). Although it is difficult to see on the graph, there is a long-range attraction and the energy has a minima at $h \approx 0.25$.

VII. CREATION OF WALLS USING EXTERNAL FIELDS

We have seen that non-Ising walls can exist and that there are stable non-Ising wall-wall pairs. We will now try to generate these interesting configurations by starting from a simpler initial field and applying an external electric field. To model this, the term

$$-E(x, t) \cdot P, \quad (54)$$

is added to the free energy (24). The electric field encourages the polarization vector to point in its direction and so we can use it to construct any desired configuration. We will turn on a specific electric field for a short burst, then turn it off and continue to flow the fields. The process is considered a success if final state is our desired one.

We begin by taking an Ising wall and applying an electric field to try and change it into a non-Ising wall. We will consider a case previously discussed: the tetragonal wall with orientation $s = (1/\sqrt{2}, 1/2, 1/2)$ and $T = 300$ K first seen in Fig. 5. In the Cartesian basis, the wall connects the vacua $(p^f, 0, 0)$ and $(-p^f, 0, 0)$. There is a stable Néel wall, with center-value approximately equal to $1/\sqrt{2}(0, p^f, p^f)$. Hence our initial state is an Ising wall, and we apply the external field

$$E_{ext}(s, t) = \begin{cases} (0, E, E) & -s_0 < s < s_0, t < t_0 \\ 0 & \text{otherwise} \end{cases}. \quad (55)$$

We take $t_0 = 5$ and $s_0 = 2.6$ nm. The wall changes from an Ising to a Néel wall provided that $E > 0.32$ MV/m. One could apply this mechanism to a poled sample material. The poled material likely has Ising walls, or non-Ising walls with equal non-Ising component. One could apply an external electric field (55) across the walls (with positive and negative E), creating an intertwined structure, like that seen in Fig. 10 (bottom right). Our analysis suggests that this new structure should be more stable than the originally poled sample.

Next we consider the stable wall-wall pair P^W seen in Fig. 9. This exists in the orthorhombic phase at $T = 250$ K and wall $s = (1, 1, 1)/\sqrt{3}$. We'll take the initial state to be the constant vacuum. The final state passes near four vacua, from $(1, 1, 0)$ to $(1, -1, 0)$ to $(-1, -1, 0)$ to $(-1, 1, 0)$ (in units of p^f) and back to the start. We need a more complicated external field to generate the more complicated configuration. We take

$$E_{ext}(s, t) = \begin{cases} (-E, 0, 0) & -s_0 < s < 0, t < t_0 \\ (E, 0, 0) & 0 < s < s_0, t < t_0 \\ 0 & \text{otherwise} \end{cases} \quad (56)$$

with $s_0 = 6$ nm. The stable P^W configuration is generated and stabilizes provided $E > 14$ MV/m. This is an order of magnitude larger than the field required to change the nature of a wall since we are creating walls from the vacuum. We have

shown that non-Ising and wall-wall pairs can be generated using an external electric field stencil.

VIII. SUMMARY

In summary, we have calculated the energy-minimizing domain walls for all possible wall orientations in perfectly-screened barium titanate. In every phase, we found orientations which support non-Ising walls. Many of these were superpositions of shorter walls. By studying the asymptotic form of the walls, we investigated the stability of multi-wall configurations. Most interestingly, we found the effect of domain wall clustering. Their stability can be explained by the existence of an effective topology. We developed tools to calculate their linear and nonlinear stability: allowing the study of their collapse. Finally, we found the required external electric field to create the non-Ising configurations.

The methods developed here can be applied to topological defects in higher dimensions with minimal adjustment.

The stability of domain walls clusters, as well as the fact that they can be created on demand by the protocol that we outline, suggests that the walls are not only the objects of academic interest but also can be used in memory applications. The most promising candidates are the neutral clusters, which we found in the rhombohedral phase. These are most likely to be stable in real barium-titanate.

Our formalism for domain walls in arbitrary orientations applies to all perfectly screened ferroelectric Ginzburg-Landau-Devonshire models, simply with different material constants. Hence it is simple to repeat the analysis for other materials such as PZT, lithium niobate, and lithium tantalate.

ACKNOWLEDGMENTS

We thank Katia Gallo, Anton Talkachov, Albert Samoilenka, Mats Barkman, and Sahal Kaushik for useful discussions. C.H. is supported by the Carl Trygger Foundation through the grant CTS 2025. This work is supported by the Swedish Research Council Grant No. 2022-04763 and by the Knut and Alice Wallenberg Foundation through the Wallenberg Center for Quantum Technology (WACQT).

APPENDIX: MATERIAL CONSTANTS

In this Appendix, we write down the material constants used in the text, and how their commonly used form relates to our tensors.

We take the potential material constants α derived in Ref. [39], except for α_{123} which comes from Ref. [40]. The elastic constants C , Q (and hence q) are the same as those used in Ref. [31]. There are slightly improved constants available in Ref. [41] but we felt it was more important to have our work directly comparable to similar theoretical studies. There is more uncertainty in the value of the derivative energy tensor G . We use the parameters proposed in Ref. [31] (note that our α_{11} and α_{12} is equal to their $\alpha_{11}^{(e)}$ and $\alpha_{12}^{(e)}$). All the parameters can be found in Table II.

TABLE II. The material constants used in this paper.

Const.	Value	Units
α_1	$3.34(T - 381)$	10^5 J m C^{-2}
α_{11}	$4.69(T - 393) - 202$	$10^6 \text{ J m}^5 \text{ C}^{-4}$
α_{12}	3.23	$10^8 \text{ J m}^5 \text{ C}^{-4}$
α_{111}	$-55.2(T - 393) + 2760$	$10^6 \text{ J m}^9 \text{ C}^{-6}$
α_{123}	4.91	$10^9 \text{ J m}^9 \text{ C}^{-6}$
α_{112}	4.47	$10^9 \text{ J m}^9 \text{ C}^{-6}$
C_{11}	2.75	10^{11} J m^{-3}
C_{12}	1.79	10^{11} J m^{-3}
C_{44}	5.43	10^{10} J m^{-3}
q_{11}	1.42	$10^{10} \text{ J m C}^{-2}$
q_{12}	-7.4	10^8 J m C^{-2}
q_{44}	1.57	10^9 J m C^{-2}
G_{11}	51	$10^{-11} \text{ J m}^3 \text{ C}^{-2}$
G_{12}	-2	$10^{-11} \text{ J m}^3 \text{ C}^{-2}$
G_{44}	2	$10^{-11} \text{ J m}^3 \text{ C}^{-2}$

We bundle the parameters into tensors as follows:

$$\begin{aligned}
 A_{ij} &= \delta_{ij}\alpha_1, \\
 A_{ijkl} &= (\alpha_{11} - \frac{1}{2}\alpha_{12})\delta_{ijkl} + \frac{\alpha_{12}}{6}(\delta_{ij}\delta_{kl} + \delta_{ik}\delta_{jl} + \delta_{il}\delta_{jk}), \\
 A_{ijklmn} &= (\alpha_{111} - \alpha_{112} + \frac{1}{3}\alpha_{123})\delta_{ijklmn} \\
 &\quad + \frac{1}{6}a_{123}\delta_{ij}\delta_{kl}\delta_{mn} \\
 &\quad + (\frac{1}{15}a_{112} - \frac{1}{30}a_{123})(\delta_{ij}\delta_{klmn} + 14 \text{ perms}).
 \end{aligned}$$

The tensors C and G have the same decomposition. We give it for C ,

$$\begin{aligned}
 C_{ijkl} &= (C_{11} - C_{12} - 2C_{44})\delta_{ijkl} + C_{12}\delta_{ij}\delta_{kl} \\
 &\quad + C_{44}(\delta_{ik}\delta_{jl} + \delta_{il}\delta_{jk}),
 \end{aligned}$$

while q and Q are similar but slightly modified,

$$\begin{aligned}
 q_{ijkl} &= (q_{11} - q_{12} - q_{44})\delta_{ijkl} + q_{12}\delta_{ij}\delta_{kl} \\
 &\quad + \frac{1}{2}q_{44}(\delta_{ik}\delta_{jl} + \delta_{il}\delta_{jk}).
 \end{aligned}$$

- [1] X. R. Huang, X. B. Hu, S. S. Jiang, and D. Feng, Theoretical model of 180° domain-wall structures and their transformation in ferroelectric perovskites, *Phys. Rev. B* **55**, 5534 (1997).
- [2] M. Taherinejad, D. Vanderbilt, P. Marton, V. Stepkova, and J. Hlinka, Bloch-type domain walls in rhombohedral BaTiO_3 , *Phys. Rev. B* **86**, 155138 (2012).
- [3] D. Lee, R. K. Behera, P. Wu, H. Xu, Y. L. Li, S. B. Sinnott, S. R. Phillpot, L. Q. Chen, and V. Gopalan, Mixed Bloch-Néel-ising character of 180° ferroelectric domain walls, *Phys. Rev. B* **80**, 060102(R) (2009).
- [4] Y. Gu, M. Li, A. N. Morozovska, Y. Wang, E. A. Eliseev, V. Gopalan, and L.-Q. Chen, Flexoelectricity and ferroelectric domain wall structures: Phase-field modeling and dft calculations, *Phys. Rev. B* **89**, 174111 (2014).
- [5] X.-K. Wei, C.-L. Jia, T. Sluka, B.-X. Wang, Z.-G. Ye, and N. Setter, Néel-like domain walls in ferroelectric $\text{Pb}(\text{Zr,Ti})\text{O}_3$ single crystals, *Nat. Commun.* **7**, 12385 (2016).
- [6] S. Cherifi-Hertel, H. Bulou, R. Hertel, G. Taupier, K. D. H. Dorkenoo, C. Andreas, J. Guyonnet, I. Gaponenko, K. Gallo, and P. Paruch, Non-ising and chiral ferroelectric domain walls revealed by nonlinear optical microscopy, *Nat. Commun.* **8**, 15768 (2017).
- [7] E. A. Eliseev, P. V. Yudin, S. V. Kalinin, N. Setter, A. K. Tagantsev, and A. N. Morozovska, Structural phase transitions and electronic phenomena at 180° -degree domain walls in rhombohedral BaTiO_3 , *Phys. Rev. B* **87**, 054111 (2013).
- [8] P. V. Yudin, A. K. Tagantsev, E. A. Eliseev, A. N. Morozovska, and N. Setter, Bichiral structure of ferroelectric domain walls driven by flexoelectricity, *Phys. Rev. B* **86**, 134102 (2012).
- [9] P. Sharma, Q. Zhang, D. Sando, C. H. Lei, Y. Liu, J. Li, V. Nagarajan, and J. Seidel, Nonvolatile ferroelectric domain wall memory, *Sci. Adv.* **3**, e1700512 (2017).
- [10] H. Sun, J. Wang, Y. Wang, C. Guo, J. Gu, W. Mao, J. Yang, Y. Liu, T. Zhang, T. Gao *et al.*, Nonvolatile ferroelectric domain wall memory integrated on silicon, *Nat. Commun.* **13**, 4332 (2022).
- [11] J. Ma, J. Ma, Q. Zhang, R. Peng, J. Wang, C. Liu, M. Wang, N. Li, M. Chen, X. Cheng *et al.*, Controllable conductive readout in self-assembled, topologically confined ferroelectric domain walls, *Nat. Nanotechnol.* **13**, 947 (2018).
- [12] J. Jiang, Z. L. Bai, Z. H. Chen, L. He, D. W. Zhang, Q. H. Zhang, J. A. Shi, M. H. Park, J. F. Scott, C. S. Hwang *et al.*, Temporary formation of highly conducting domain walls for non-destructive read-out of ferroelectric domain-wall resistance switching memories, *Nat. Mater.* **17**, 49 (2018).
- [13] Y. Ishibashi and E. Salje, A theory of ferroelectric 90° degree domain wall, *J. Phys. Soc. Jpn.* **71**, 2800 (2002).
- [14] M. Finazzi, M. Savoini, A. R. Khorsand, A. Tsukamoto, A. Itoh, L. Duo, A. Kirilyuk, T. Rasing, and M. Ezawa, Laser-induced magnetic nanostructures with tunable topological properties, *Phys. Rev. Lett.* **110**, 177205 (2013).
- [15] X. Zhang, J. Xia, Y. Zhou, D. Wang, X. Liu, W. Zhao, and M. Ezawa, Control and manipulation of a magnetic skyrmionium in nanostructures, *Phys. Rev. B* **94**, 094420 (2016).
- [16] S. Zhang, F. Kronast, G. van der Laan, and T. Hesjedal, Real-space observation of skyrmionium in a ferromagnet-magnetic topological insulator heterostructure, *Nano Lett.* **18**, 1057 (2018).
- [17] F. N. Rybakov and N. S. Kiselev, Chiral magnetic skyrmions with arbitrary topological charge, *Phys. Rev. B* **99**, 064437 (2019).
- [18] D. Foster, C. Kind, P. J. Ackerman, J.-S. B. Tai, M. R. Dennis, and I. I. Smalyukh, Two-dimensional skyrmion bags in liquid crystals and ferromagnets, *Nat. Phys.* **15**, 655 (2019).
- [19] M. Barkman, A. Samoilenka, T. Winyard, and E. Babaev, Ring solitons and soliton sacks in imbalanced fermionic systems, *Phys. Rev. Res.* **2**, 043282 (2020).
- [20] J. Garaud, M. N. Chernodub, and D. E. Kharzeev, Vortices with magnetic field inversion in noncentrosymmetric superconductors, *Phys. Rev. B* **102**, 184516 (2020).

- [21] A. Samoilenka and E. Babaev, Spiral magnetic field and bound states of vortices in noncentrosymmetric superconductors, *Phys. Rev. B* **102**, 184517 (2020).
- [22] J. Garaud, J. Carlström, E. Babaev, and M. Speight, Chiral $\mathbb{C}P^2$ skyrmions in three-band superconductors, *Phys. Rev. B* **87**, 014507 (2013).
- [23] H.-L. Hu and L.-Q. Chen, Computer simulation of 90 ferroelectric domain formation in two-dimensions, *Mater. Sci. Eng. A* **238**, 182 (1997).
- [24] H.-L. Hu and L.-Q. Chen, Three-dimensional computer simulation of ferroelectric domain formation, *J. Am. Ceram. Soc.* **81**, 492 (1998).
- [25] P. Marton, I. Rychetsky, and J. Hlinka, Domain walls of ferroelectric BaTiO₃ within the ginzburg-landau-devonshire phenomenological model, *Phys. Rev. B* **81**, 144125 (2010).
- [26] M. A. Lohe, Soliton structures in $p(\varphi)_2$, *Phys. Rev. D* **20**, 3120 (1979).
- [27] P. Dorey, K. Mersh, T. Romanczukiewicz, and Y. Shnir, Kink-antikink collisions in the ϕ^6 model, *Phys. Rev. Lett.* **107**, 091602 (2011).
- [28] V. A. Gani, A. E. Kudryavtsev, and M. A. Lizunova, Kink interactions in the (1 + 1)-dimensional ϕ^6 model, *Phys. Rev. D* **89**, 125009 (2014).
- [29] A. Alonso-Izquierdo, Non-topological kink scattering in a two-component scalar field theory model, *Commun. Nonlinear Sci. Numer. Simul.* **85**, 105251 (2020).
- [30] R. A. Battye and P. M. Sutcliffe, Symmetric skyrmions, *Phys. Rev. Lett.* **79**, 363 (1997).
- [31] J. Hlinka and P. Márton, Phenomenological model of a 90° domain wall in BaTiO₃-type ferroelectrics, *Phys. Rev. B* **74**, 104104 (2006).
- [32] V. Stepkova, P. Marton, and J. Hlinka, Ising lines: Natural topological defects within ferroelectric bloch walls, *Phys. Rev. B* **92**, 094106 (2015).
- [33] C. Halcrow and E. Babaev, Stable kink-kink and metastable kink-antikink solutions, *SIGMA* **19**, 34 (2023).
- [34] P. V. Yudin, A. K. Tagantsev, and N. Setter, Bistability of ferroelectric domain walls: Morphotropic boundary and strain effects, *Phys. Rev. B* **88**, 024102 (2013).
- [35] C. Barnes and N. Turok, A technique for calculating quantum corrections to solitons, [arXiv:hep-th/9711071](https://arxiv.org/abs/hep-th/9711071).
- [36] S. B. Gudnason and C. Halcrow, Vibrational modes of skyrmions, *Phys. Rev. D* **98**, 125010 (2018).
- [37] Weinan E, W. Ren, and E. Vanden-Eijnden, Simplified and improved string method for computing the minimum energy paths in barrier-crossing events, *J. Chem. Phys.* **126**, 164103 (2007).
- [38] A. Benfenati, A. Maiani, F. N. Rybakov, and E. Babaev, Vortex nucleation barrier in superconductors beyond the bean-livingston approximation: A numerical approach for the sphaleron problem in a gauge theory, *Phys. Rev. B* **101**, 220505(R) (2020).
- [39] W. Buessem, L. Cross, and A. Goswami, Phenomenological theory of high permittivity in fine-grained barium titanate, *J. Am. Ceram. Soc.* **49**, 33 (1966).
- [40] A. J. Bell and L. E. Cross, A phenomenological gibbs function for BaTiO₃ giving correct e field dependence of all ferroelectric phase changes, *Ferroelectrics* **59**, 197 (1984).
- [41] M. Zgonik, P. Bernasconi, M. Duelli, R. Schlessler, P. Günter, M. H. Garrett, D. Rytz, Y. Zhu, and X. Wu, Dielectric, elastic, piezoelectric, electro-optic, and elasto-optic tensors of BaTiO₃ crystals, *Phys. Rev. B* **50**, 5941 (1994).